Hydrodynamics Analysis on the High-Speed Surface Vehicle with Super-Cavitating Hydrofoils

S. Zhao, M. Xiang[†], H. Zhou, and W. Zhang

College of Aerospace Science and Engineering, National University of Defense Technology, Changsha, Hunan, 410073, P.R. China

† Corresponding Author Email: xiangmin333@hotmail.com

ABSTRACT

Expeditiously transferring personnel or cargo between seashores or vessels becomes an imperative requirement in ocean engineering. In this paper a novel high-speed surface vessel which has two symmetrical under-water torpedo-shaped sub-water bodies connected to the hull with two couples of super-cavitating hydrofoils, which are located in series along the axis of the body, has been proposed. By using supercavitation technology in the sub-water body and the hydrofoil, this vessel could achieve extreme high speed. Considering the sophisticated configuration and the complex flow field around the vessel, this paper has investigated on the hydrodynamics of this vehicle through numerical simulation. The numerical method which couples the Schnerr and Sauer cavitation model into the mixture multiphase model has been validated by the case of two-dimensional super-cavitating hydrofoil. Then simulation has been carried out for this novel vehicle with different wetting depths. Based on analysing details of the flow structure, the there-dimensional effect for the super-cavitating hydrofoil, as well as the interaction between the fore and the aft hydrofoils has been revealed. Then the hydrodynamics curves for both the fore and the aft hydrofoils are obtained, providing guidance for the design of the serial hydrofoils. Furthermore, hydrodynamic analysis has been made for the sub-water body under the effect of hydrofoils. This work may give meaningful references for the design of high-speed surface vehicles.

Keywords: Numerical simulation; Hydrofoil; Supercavitation; Hydrodynamics

1. INTRODUCTION

High speed underwater and surface vehicles are urgently required to enhance the ability of ocean resource observation, exploration and application. SWATH (small-waterplane-areatwin-hull ship) Gore (1985), Begovic *et al*. (2015), Chao *et al*. (2016), which is characterized by a small waterplane area and two sub-water demihulls, has good seakeeping behavior with higher natural periods in heave and pitch Faltinsen (2005). However, due to the large wet area, the performance of SWATH in high-speed state is not satisfying. New types of combined surface vehicles, such as HYSWATH (hydrofoil small-waterplane-area-twin-hull ship), has been proposed to increase the speed and stability in relatively rough seas. This novel configuration takes advantage of the both the SWATH and the hydrofoil ship Petkie (1971), Faison (2014) which could decrease the resistance by reducing the wet surface of the hull. Researches have been made on the configuration and hydrodynamics of this kind of surface vehicle. Jin (2005) has investigated on the hull form generation, resistance performance, pitching performance and other realms of HYSWATH. Farahani (2016) used Star-CCM+ calculation software to study the influence of gravity center and demi hull spacing on its resistance performance, which is of great importance for the design of HYSWATHs. Georgiadis (2014) recently proposed a hybrid design which combines SWATH with those of surface-piercing (SP) and super-cavitating (SC) hydrofoils. It works at two different modes, one of which is the displacement mode when SWATH hulls provide buoyancy, and the other one is the foil borne mode when the lift mainly comes from its under-water rotatable hydrofoils.

It suggests that to achieve higher speed, both the configuration and drag reduction technology play critical roles for the surface vehicles. In this research, a new type of vessel, which originates from SWATH as well, has been proposed to serve as a high-speed experimental platform. It is composed of a main central body with its keel line suspended above sea level, two sub-water torpedo-liked bodies and two couples of super-cavitating hydrofoils. The hydrofoils not only connect the central part to the sub-water part, but also provide lift to balance the weight. Both the hydrofoil and the sub-water part use

supercavitation technology to increase the speed of the platform. In order to predict the hydrodynamics precisely, it is of great importance to figure out the performance of the super-cavitating hydrofoils, which act as a kernel component of the whole vehicle, and their interaction with other parts.

In early stage the design of hydrofoils are focused on working in full wet flow without cavitation. However, as the vehicle achieves higher speed when cavitation occurs, the normal hydrofoil can't meet the requirements due to its instability un-der cavitation Auslaender (1962). After the request for stable control on super-cavitating vehicles such as high-speed torpedos, the devises and researches of new hydrofoils were brought out. The super-cavitating hydrofoils are designed to provide more stable cavities, compared to the traditional low-speed hydrofoils, at lower cavitation number. The pressure inside the cavity is lower than that in water, providing the possibility to reduce the pressure drag and increase the lift. Different types of hydrofoils performs differently. Super-cavitating hydrofoils in Long and Daybell (1961) with sharp leading edge and trailing edge are designed. Two super-cavitating hydrofoil models in Baker (1975), TAP-1 and TAP-2, have been designed, which are proved effective under high cruise speed (around 80 knot-s). In recent years, S. Brizzolara and L. Bonfiglio has devised a new SCSB family of super-cavitating hydrofoils in Brizzolara and Bonfiglio (2015) and compared its performance with NACA-65 pro-file using numerical simulation. A novel high-speed hydrofoil in Brizzolara (2015), which has a main body connected to the tail through two right angle chamfers, has been designed and applied in HYSWATH. It has optimal performance both in super-cavitating conditions and in precavitating conditions (including transitional regime). Pursuing for wider region of angel of attack and cavitation number, symmetrical wedge-shaped hydrofoils in Zhang *et al.* (2014) are applied in engineering. Other modified or combined wedge-shaped hydrofoils are still under design. For the interaction between hydrofoils, relevant researches have started in these years. Three 2D hydrofoils located in a cascade Lohrberg *et al.* (2002) have been investigated by both numerical simulation and experimental means, where strong interaction among these cavities and the coupling frequency was studied. When it comes to the performance of hydrofoils un-der free surface, analysis based on BEM (Boundary Element Method) in Bal (2007), Lee *et al.* (1994), Pearce and Brandner (2007) has been done. Based on the results, the Froude number, cavitation number as well as submerged depth (or wet surface) should be seriously considered.

Considering the sophisticated configuration and the complex flow field around the vessel, this paper will investigate on the hydrodynamics of this new type of surface vehicle through numerical simulation. As the aerodynamics forces

occupies much less proportion than that of hydrodynamics, we merely take the sub-water part and hydrofoils into account, regardless of the part above the water surface in this paper. Focus will be laid on understanding the interaction among hydrofoils and the sub-water part. This research may provide useful guidance for the overall design of high-speed surface vehicle in the future.

2. NUMERICAL METHODS AND MODEL PARAMETERS

2.1 Governing Equations

In our study, the homogeneous multiphase model, which combines incompressible single phase Navier-Stokes equations and Mixture multiphase model, is applied for the simulation. Both vapor and liquid phases share the same velocity and pressure field. The local mixture properties can be calculated based on the single state of each phase. The viscosity and density of the mixture can be expressed as:

$$\mu_m = \alpha_l \mu_l + \alpha_v \mu_v \tag{1}$$

$$\rho_m = \alpha_l \rho_l + \alpha_v \rho_v \tag{2}$$

Where subscripts m, l and v refer to phases of mixture, liquid and vapor respectively. α_k is the volume fraction of phase $k. u = (\alpha_l \rho_l u_l + \alpha_v \rho_v u_v) / \rho_m$ is the mass-averaged velocity component.

Disregarding the effects of gravity, drift velocity and surface tension, the continuity equation can be written as follows:

$$\frac{\partial \rho_m}{\partial t} + \frac{\partial}{\partial x_i}(\rho_m u_i) = 0 \tag{3}$$

The momentum equation for the mixture can be obtained by summing the individual momentum equations for all phases, which can be expressed as

$$\frac{\partial(\rho_m u_i)}{\partial t} + \frac{\partial(\rho_m u_i u_j)}{\partial x_j} = \\ -\frac{\partial p}{\partial x_i} + \frac{\partial}{\partial x_j}\left[\mu_m\left(\frac{\partial u_i}{\partial x_j} + \frac{\partial u_j}{\partial x_i}\right)\right] \tag{4}$$

Where p is the pressure, and i and j are component directions in Cartesian coordinates.

2.2 Cavitation Model

In this article the Schnerr and Sauer cavitation model in Schnerr and Sauer (2001), Ansys Inc. (2011) has been used for the simulation. Based on the bubble dynamics put forward by Rayleigh in 1917, this cavitation model solves the Rayleigh equation for modelling of growth and collapse of vapor regimes. We give the saturated vapor pressure as 3540Pa. Using the following expression, the vapor volume fraction and the number of bubbles per volume of liquid are

connected:

$$\alpha_v = \frac{\frac{4}{3}\pi \mathfrak{R}_B^3 n}{1+\frac{4}{3}\pi \mathfrak{R}_B^3 n} \qquad (5)$$

Where $\mathfrak{R}_B$ is the bubble radius and $n = 10^{13}$ the constant bubble number density. We set the initial radius of the vapor nucleus as 10^{-6}m, and the initial volume fraction of the vapor content α_v can be determined. Following the derivation, the volume fraction equation for vapor phase can be obtained:

$$\frac{\partial}{\partial t}\left(\alpha_v \rho_v\right) + \frac{\partial \left(\alpha_v \rho_v u_{vj}\right)}{\partial x_j} = \frac{\rho_v \rho_l}{\rho_m}\frac{D\alpha_v}{Dt} = R \qquad (6)$$

Here R refers to the mass transfer rate term. The following equations for phase transition were derived by Schnerr and Sauer:

$$R = \frac{\rho_v \rho_l}{\rho_m}\alpha_v\left(1-\alpha_v\right)\frac{3}{\mathfrak{R}_B}\sqrt{\frac{2}{3}\frac{p-p_v}{\rho_l}} \qquad (7)$$

$$\mathfrak{R}_B = \sqrt[3]{\frac{\alpha_v}{1-\alpha_v}\frac{3}{4\pi}\frac{1}{n}} \qquad (8)$$

2.3 Turbulence Model

For most industrial problems, the cavitation phenomena are usually high Reynolds number flow and the turbulence is an important issue. The Realizable $k-\varepsilon$ turbulence model Ansys Inc. (2011) has been adopted in our simulation.

The transportation equations of k and ε are as follows

$$\frac{\partial}{\partial t}\left(\rho_m k\right) + \frac{\partial}{\partial x_j}\left(\rho_m k u_j\right) = \frac{\partial}{\partial x_j}\left[\left(\mu_m + \frac{\mu_t}{\sigma_k}\right)\frac{\partial k}{\partial x_j}\right]$$
$$+ G_k + G_b - \rho_m \varepsilon - Y_M + S_k \qquad (9)$$

$$\frac{\partial}{\partial t}\left(\rho_m \varepsilon\right) + \frac{\partial}{\partial x_j}\left(\rho_m \varepsilon u_j\right) = \frac{\partial}{\partial x_j}\left[\left(\mu_m + \frac{\mu_t}{\sigma_\varepsilon}\right)\frac{\partial \varepsilon}{\partial x_j}\right]$$
$$+\rho_m C_1 S\varepsilon - \rho_m C_2 \frac{\varepsilon^2}{k+\sqrt{v\varepsilon}} + C_{1\varepsilon}\frac{\varepsilon}{k}C_{3\varepsilon}G_b + S_\varepsilon \qquad (10)$$

Where

$$C_1 = \max\left[0.43,\frac{\eta}{\eta+5}\right], \eta = S\frac{k}{\varepsilon}, S = \sqrt{2S_{ij}S_{ij}}$$

Table 1 Constants of realizable $-\varepsilon$ model

$C_{1\varepsilon}$	C_2	σ_k	σ_ε
1.44	1.9	1.0	1.2

Table 2 Case description

case No.	1	2	3	4
wetting depth of hydrofoils (mm)	80	100	120	none

G_k represents the generation of turbulence kinetic energy due to the mean velocity gradients, and G_b is the generation of turbulence kinetic energy due to buoyancy. In this case, $Y_M = 0$ in incompressible flow. S_k and S_ε are user-defined source terms, which are set zero as well. σ_k and σ_ε are constant turbulent Prandtl numbers for k and ε respectively. Compared to the standard k-ε turbulence model in Ansys Inc. (2011), μ_t is no longer a constant, and it is calculated but $\mu_t = \rho_m C_\mu\frac{k^2}{\varepsilon}$, in which C_μ is not a constant by a complicated function. The constants of the model are listed in the Table.1.

2.4 Geometry Description

We hereby, neglecting its transverse motion, simulate half of the under-water part aiming to reduce the amount of the mesh. The geometry for our simulation is composed of a sub-water axisymmetric body and a set of super-cavitating hydrofoils as shown in Fig. 1. The hydrofoils are located in the fore and aft part of the sub-water body respectively. The plane where the chord of the hydrofoils lie is 45 degrees oblique to the horizontal water surface. The TAP-1 profile in Baker (1975) which is supposed to be in feasible condition passed by high speed water flow of around 80 knots is chosen for the super-cavitating hydrofoils. The attack angle of both super-cavitating hydrofoils are set as 5 degrees. All the sub-water bodies in these cases are set with the same length L = 600mm and a small cavitator with D = 25mm on the head of the body. Simulation are carried out for the platform with different wetting depth which is defined in Fig. 1. Details of these cases are all shown in the Table.2, where case 4 contains a single body without hydrofoils in the same depth as case 2.
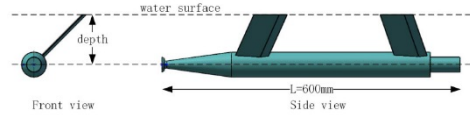

Fig. 1. Geometry of the sub-water body

2.5 Numerical Methods and Boundary Conditions

Based on the FVM (finite-volume method) with a coupled scheme by applying the commercial computational fluid dynamics software ANSYS Fluent, the numerical simulations are performed. The Mixture multiphase model as well as Schnerr and Sauer cavitation model are adopted. The scheme SIMPLE is selected for the pressure-velocity coupling. The equations are discretized by second order up-wind in space. We set the solution method as time steady. Figure. 2 shows the computational domain of the 3D calculation. The inlet velocity varies from 10 to 50m/s in X direction. The cavitation number σ can be obtained by $\sigma = \left(p_\infty - p_v\right)/\frac{1}{2}\rho v_\infty^2$. Moving wall boundaries are imposed on the bottom and side-walls of the computational domain. Full scale Raynold number $Re = Vc/v = O(10^7)$ is adopted.

Considering the physical features, which indicates that the vectors do not pass through it and scalars have no gradient on the water surface, the boundary is set as symmetry plane. The whole region is discretized into about 8 million hexahedral elements with good orthogonality and quality, as shown in the Fig. 3. The computational domain is big enough for stable calculation for incompressible flow. The model is fixed while the water flows towards the body.
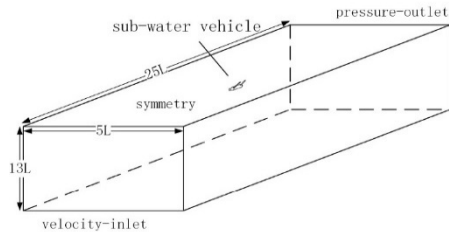

Fig. 2. Computing domain and boundary conditions
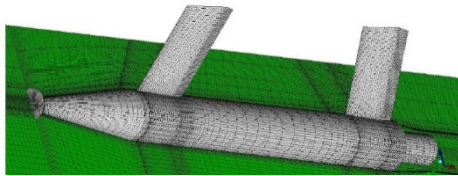
Fig. 3. Mesh around the sub-water body

2.6 Validation and Verification

Considering the lack of relative computational or experimental data for both the TAP-1 hydrofoil and this certain configuration, alternatively we hereby simulate the hydrodynamic coefficient of another 2D super-cavitating hydrofoil in Parkin (1956) using the same numerical methods mentioned above. Figure. 4 gives a clear view of the comparison of the results from our numerical simulation and the original experimental data in Parkin (1956) at 7 degrees angle of attack. At non-cavitating regime for σ > 0.8 the lift and drag coefficient remains nearly the same. It is seen that for the state where σ < 0.8, the lift coefficient drops from around 0.7 to 0.25, and the drag coefficient keeps mainly constant with minor fluctuation. Obviously the two results match well, with only minor differences. The cavity shapes for different cavitation numbers are also shown by the contour of void fraction. These results are found to agree well with the existing results. Thus the cavitation model and numerical methods used in this article are proved reasonable and reliable.

3. NUMERICAL RESULTS AND ANALYSIS

3.1 Flow Structure Analysis

In this subsection we take case 3 as an example to show the detailed multiphase flow structure. The iso-surface of water volume of fraction $\alpha_l = 0.5$ under different cruising speed is displayed in Fig. 5. Several minor detached cavities can be observed near hydrofoils in (a) and (b). Four partial cavities exist around the whole body, two
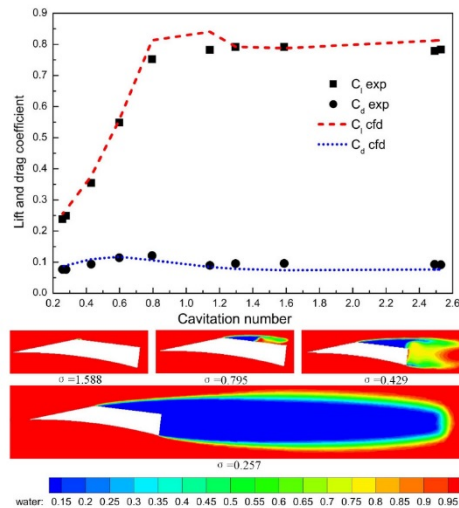

Fig. 4. Comparison of experimental data and numerical simulation results for 2D Circular Arc hydrofoil, countour of void fraction around circular arc

of which are generated from the suction side of the hydrofoil while the others are generated from the sub-water part. As the increase of the cruise speed, all the cavities expand, resulting obvious interaction between the cavity on the sub-water body surface and the cavity on the hydrofoil surface. As shown in the figure, the cavity which goes after the upstream hydrofoil is larger than that of the downstream one. At higher speed, the cavity generated by the fore hydrofoil extends to the surface of the aft hydrofoil. A non-axis-symmetric cavity is also observed partially coving the sub-water body surface due to the interference from the fore hydrofoil.
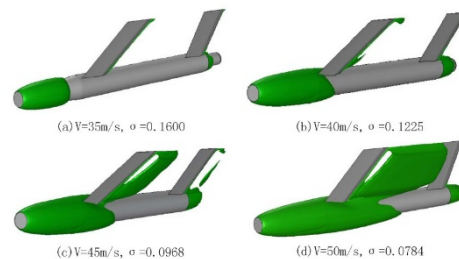

Fig. 5. Cavity shape development under different cruising speed

Figure. 6 gives a clear pressure distribution contour of the body at $V = 45$m/s. High-pressure regions can be seen at the leading edge of both the front and aft hydrofoils which are mainly induced by the flow stagnation. The other two high-pressure regions exist downstream of the hydrofoils which are caused by the collapse of the cavity or the flow deceleration at the cavity trailing edge. In comparison with the fore hydrofoil, the upstream high-pressure region of the aft hydrofoil is strengthened due to the collapse of the front cavity. This will have an effect to increase the local cavitation number and suppress the cavitation on the aft hydrofoil. Inside the cavity which covers the suction side and trailing edge of the hydrofoil, the pressure maintains at 3540Pa. For the sub-water body, the

high-pressure regions exist at both the head of the cavitator and the end of the partial cavity. The non-axis-symmetry for the pressure is also observed which is in accordance with the volume fraction of vapor distributions.

3.2 Hydrodynamics Analysis of Super Cavitating Hydrofoils

3.2.1 Three Dimensional Effect and Interaction Analysis Between Hydrofoils

In this subsection we set to analysis and estimate the performance of fore and aft hydrofoils. Due to the intense interaction among hydrofoils and the sub-water body, obvious three dimensional effect is observed for the flow parameters around the hydrofoils. Figure. 7 displays the volume fraction contours on three cut planes of the fore hydrofoil at σ = 0.2177 and σ = 0.0968. It is observed that in Fig. 7 (a), the distribution of volume fraction along the span direction is non-uniform. For the 2D hydrofoil, the cavitation originates from both the tail and the leading edge, forming a transparent cavity. However, for the 3D hydrofoils the cavitation at all sections are greatly depressed, especially for the subsection (cut 1) close to the sub-water part, where no cavitation occurs on the suction side and only cavitation bubbles exist at the tail.
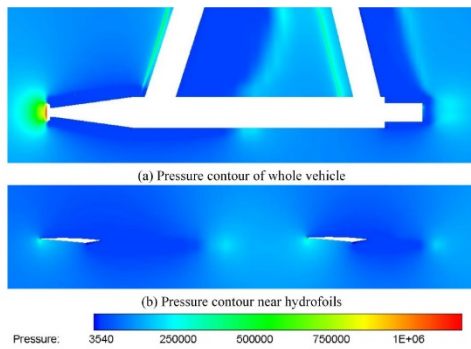

(a) Pressure contour of whole vehicle

(b) Pressure contour near hydrofoils

Fig. 6. Pressure distribution of case 3

At higher speed in Fig. 7 (b), the cavity length at the hydrofoil tail is decreased evidently in comparison with the 2D figure. For the section close to the sub-water body surface, the cavity on the hydrofoil surface merges with the partial cavity from the sub-water body, forming a large cavity covering part of the pressure side. On middle and far side of the hydrofoil the size of cavity is almost equal, and a separation of the cavity can be observed, which is quite different from the cavity produced in 2D profile. Above all, the non-linearity of the three-dimensional cavitation may lead to difficulties in predicting the hydrofoil dynamics precisely.

As mentioned in the last subsection, the flow field around the aft hydrofoil is under great affection of the fore hydrofoil. As shown in Fig. 7, as the decrease of the cavitation number, a notable difference is observed for the cavity length generated by the fore and aft hydrofoils. Gradually, the cavity generated by the fore hydrofoil starts to interact with the surface of the
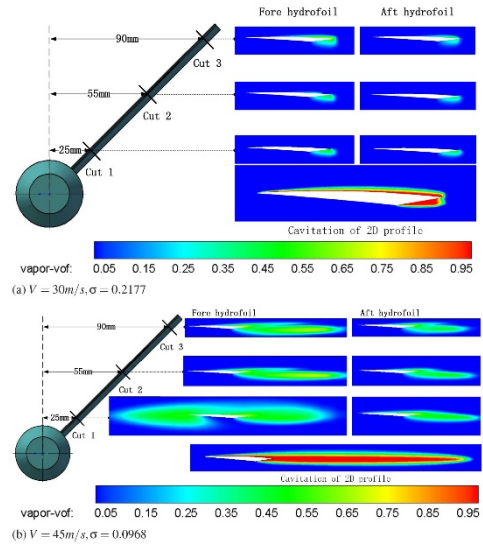

(a) $V = 30m/s, \sigma = 0.2177$

(b) $V = 45m/s, \sigma = 0.0968$

Fig. 7. Contour of volume fraction of vapor on hydrofoils for case 2

aft hydrofoil. Due to the strong vortex flow at the end of the cavity, great fluctuation may occur for the hydrodynamics of the aft hydrofoil, making it difficult for the design and control of this vehicle. Therefore, for the vehicle in our research, it will be better to work under 50m/s to avoid strong interaction between the hydrofoils. Ventilating non-condensible gas into the cavity will be required to achieve supercavitation.

3.2.2 Hydrodynamic Performance of Hydrofoils

Figure. 8 shows the lift and drag coefficient of the fore hydrofoils in case 1-3 respectively. The hydrodynamic curves for the 2D TAP-1 are also presented in the figures for better understanding on the three-dimensional effect of the hydrofoils. For the fore hydrofoils, both the drag and lift curves follow the variation trend of the 2D curves. Under high cavitation number when the hydrofoils are under full wet flow, the lift coefficient varies slightly. When the cavitation occurs on the suction side, the lift curves climb up quickly as the partial cavity expands on the suction side. When the suction side is totally covered by the cavity, the pressure difference maintains stable and the lift coefficient descends gently along with the increasing velocity. In comparison with the 2D curves, both the lift and drag curves are shifted down, which is resulted by the suppression of the pressure difference. As shown in Fig. 8, the three-dimensional curves representing different wetting depth almost coincide with each other, presenting slight difference in the high-speed region. The pattern of the C_d curves is, to some extent, similar to that of the C_l curves.

Different variation trends exist for the hydrodynamic coefficient of the aft hydrofoils. As stated in the last section, the interference from the fore hydrofoil and the sub-water body has evident influence on the hydrodynamic performance for the aft hydrofoil, making the

coefficients fluctuate.

Figure. 9 compares the lift-to-drag ratio between the fore and the aft hydrofoil in case 3. An optimum velocity exists for the hydrofoils to get the maximum lift-to-drag ratio. For the fore hydrofoil, when the cavitation starts at suction side the lift-to-drag ratio raises up dramatically before reaching the maximum value. After then it descends gradually as the cavity on the sub-water body surface extends to the pressure side of the hydrofoil. This effect act·s more obviously along with the decreasing of the wetting depth. Therefore if the sub-water body gets too close to the surface, the super-cavitating hydrofoils will work inefficiently. For the aft hydrofoil, the lift-to-drag ratio is raised up in the full wet flow under the affection of the fore one. However, as the cavitation is depressed by the fore one, the optimum cavitation number to reach the maximum lift-to-drag ratio is decreased. It suggests to adjust the angle of attack and the location for the aft hydrofoil to obtain the optimum performance at the same cruise velocity.
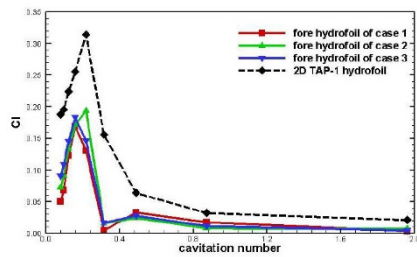
(a) Lift coefficient
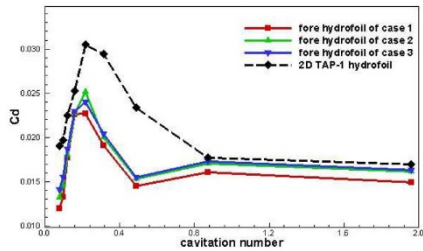
(b) Drag coefficient

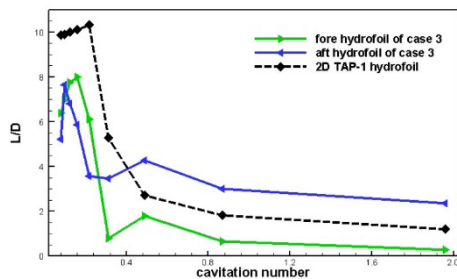**Fig. 8. Hydrodynamic coefficient of fore hydrofoils and 2D hydrofoil**

Fig. 9. Lift to drag ratio of hydrofoils of case 3 and 2D hydrofoil

3.3 Analysis on Interference from Hydrofoils to the sub-Water Body

With the interference from the hydrofoils, the flow field around the sub-water body has been altered. As Fig. 5 shows, the cavity generated by the fore hydrofoil could merge with the cavity on the surface of the sub-water body, forming a non-axisymmetric large cavity which leads to the decrease of the local viscous fraction. However, the existence of aft hydrofoil could amplify the size of the base cavity which will result in the raise of the pressure drag in the bottom. This all may induce the variation of the hydrodynamics for the sub-water body. Figure. 10 gives the pressure distribution of case 2 and case 4 on a vertical cutting plane at V = 40m/s, where the non-symmetric of the surface cavity is clearly shown. In general, the cavity length is marginally diminished by the hydrofoil.

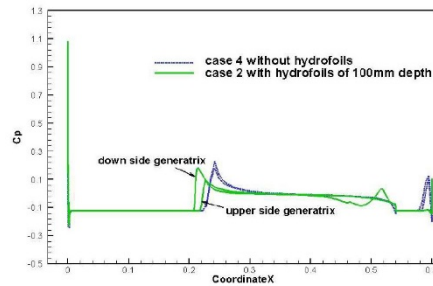**Fig. 10. Pressure distribution along the axial direction of the sub-water body surface at V = 40m/s**

Figure. 11 compares the C_d of the sub-water body part with and without hydrofoils. As shown in the figure, the wetting depth of the hydrofoils has no evident influence on the drag coefficient of the sub-water body, which is indicated by the three over-lapped curves. Under the affection of the hydrofoils, a steep drop is observed for the drag coefficient around σ = 0.1225, owing to the combination of regions of cavities. In general, the C_d curves with hydrofoils are moved up uniformly in comparison with the one without hydrofoils. For simplicity in the first-stage design, a linear modification could be used to predict the sub-water body hydrodynamics in consideration of the affections from hydrofoils. Moreover, we take a deeper insight into the component of the drag coefficient. In fig.12, four conditions under different velocities in case 2 and 4 has been analysed. Both pressure and viscous drag coefficient decreases under cavitation condition (V = 45m/s and V = 50m/s). In both case 2 and 4, the pressure drag coefficient, at higher velocity, takes a much larger part than the viscous part.

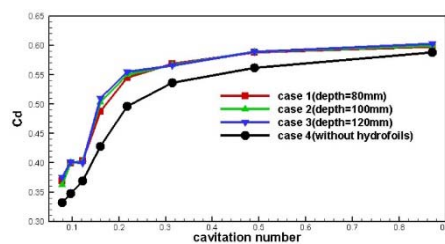**Fig. 11. Drag coefficient of sub-water body**

4. CONCLUSION

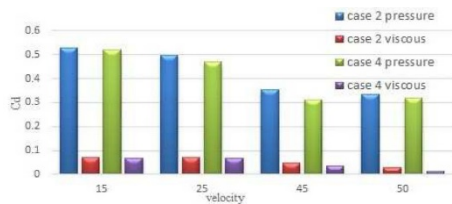This article focuses on the hydrodynamic

Fig. 12. Component of drag coefficient of sub-water part

characters on a sub-water torpedo-liked body with fore and aft hydrofoils using numerical simulation. From the results and analysis above, some useful conclusion, which is helpful for the upcoming hydrodynamic calculation and design of similar vehicles, are as follows:

1. Due to the interaction with the other parts, obvious three-dimensional effect is observed for the super-cavitating hydrofoils. The cavitation at all subsections are greatly depressed in comparison with the two-dimensional flow field, especially for the one close to the sub-water body.

2. For the aft hydrofoil, the local cavitation number is increased by the collapse of the up-stream cavity, leading to a much shorter cavity length on the hydrofoil surface in comparison with the fore one. As the decrease of the cavitation number, the cavity generated by the fore hydrofoil will extend to the surface of the aft hydrofoil, which may induce great fluctuation for the hydrodynamics.

3. For the hydrodynamic coefficients of the fore hydrofoil, both C_l and C_d, while shifted down, vary versus cavitation number in the same tendency with the 2D curve. When considering the lift to drag ratio, different optimum velocities can be observed for fore and aft hydrofoils to reach the top value of its own. For further design, the location and the angle of attack of the aft hydrofoil should be adjusted and optimized to reach the best *L/D* at the same cruise velocity with the fore hydrofoil.

4. For this configuration, on the whole, the Cd of the sub-water body drops as the inlet velocity increases. The existence of the hydrofoils may diminish the cavity size and alter the pressure distribution around the body. A linear modification could be used to predict the sub-water body hydrodynamics in consideration of the affections from hydrofoils in the primary design stage.

ACKNOWLEDGEMENT

REFERENCES

Ansys Inc. (2011). ANSYS FLUENT Theory

Baker, E. S. (1975). Notes of the design of two supercavitating hydrofoils. Report SPD-479-13, David W. Taylor Naval Ship Research and Development Center, Bethesda.

Bal, S. (2007). A numerical method for the prediction of wave pattern of surface piercing cavitating hydrofoils. In *Proceedings of the Institution of Mechanical Engineers – Part C*, Volume 221, pp. 1623–1633.

Begovic, E., C. Bertorello, and S. Mancini (2015). Hydrodynamic performances of s-mall size SWATH craft. *Brodogradnja* 66(4), 1–22.

Brizzolara, S. (2015). A new family of dual-mode super-cavitating hydrofoils. In *Fourth International Symposium on Marine Propulsors*.

Brizzolara, S. and L. Bonfiglio (2015). Compar ative CFD investigation on the performance of a new family of super-cavitating hydro-foils. *Journal of Physics: Conference Series* 656(1), 012147.

Faison, L. A. (2014). *Design of a high speed planing hull with a cambered step and surface piercing hydrofoils*. Master's thesis, Massachusetts Institute of Technology.

Faltinsen, O. M. (2005). *Hydrodynamics of high-speed marine vehicles*. Cambridge University Press.

Farahani, S. A. (2016). *Resistance performance research of hybrid hydrofoil small water area twin hull*. Thesis, Shanghai Jiao Tong University, Shanghai, China.

Georgiadis, V. (2014). *Design and assessment of a super high speed, hybrid hydrofoil/SWATH crew boat*. Massachusetts Institute of Technology.

Gore, J. L. (1985). SWATH ships. *Naval Engineers Journal* 97(2), 83–112.

Guide 12. 0 Cavitation Models. Auslaender, J. (1962). Low drag supercavitating hydrofoil sections. Technical report, Hydronautics Inc.

Jin, H. (2005). *Research on the conceptual design and performance of HYSWATH*. Thesis, Shanghai Jiao Tong University, Shang-hai, China.

Lee, C. S., C. W. Lew, and Y. G. Kim (1994). Analysis of a two-dimensional partially or supercavitating hydrofoil advancing under a free surface with a finite froude number. Pro-ceedings of the 19th Symposium on Naval Hydrodynamics, 605–618.

Lohrberg, H., B. Stoffel, R. Fortes-Patella, O. Coutier-Delgosha, and J. Reboud (2002). Numerical and experimental investigations on the cavitating flow in a cascade of hydrofoils. *Experiments in Fluids* 33(4), 578–586.

Long, T. and D. A. Daybell (1961). Water tunnel

tests of three vented hydrofoils in two dimensional flow. *Journal of Ship Research* 5(3), 1–15.

Parkin, B. R. (1956). *Experiments on circular arc and flat plate hydrofoils in noncavitating and full cavity flows*. Report 47-6, Hydrodynamics Laboratory, California Institute of Technology.

Pearce, B. W. and P. A. Brandner (2007). Limitations on 2d super-cavitating hydrofoil performance. In *Australasian Fluid Mechanics Conference*, pp. 1399–1404.

Petkie, D. A. I. (1971). Operational and developmental experience on the U.S. navy hydrofoil

High Point. *Soviet Journal of Experimental and Theoretical Physics* 50(1), 79–85.

Schnerr, G. H. and J. Sauer (2001). Physical and numerical modeling of unsteady cavitation dynamics. In *ICMF 2001- 4th International Conference on Multiphase Flow*, New Orleans, USA.

Wang, C., Y. Lin, Z. Hu, L. Geng, and D. Li (2016). Hydrodynamic analysis of a SWATH planing USV based on CFD. In *OCEANS 2016-Shanghai*, Shanghai, China, 1–4. IEEE.

Zhang, Y., X. Yuan, and F. Deng (2014). *Fluid dynamics of supercavitating underwater vehicles*. National Defense Industry Press.